

True random number generation using metastable 1T' molybdenum ditelluride

*Yang Liu, Pengyu Liu, Yingyi Wen, Zihan Liang, Songwei Liu, Lekai Song, Jingfang Pei, Xiaoyue Fan, Teng Ma, Gang Wang, Shuo Gao, Kong-Pang Pun, Xiaolong Chen, Guohua Hu**

Y. Liu, P. Liu, Y. Wen, S. Liu, L. Song, J. Pei, G. Hu (ORCID ID 0000-0001-9296-1236)
Department of Electronic Engineering, The Chinese University of Hong Kong, Shatin, N. T.,
Hong Kong S. A. R., 999077, China

Y. Liu

Shun Hing Institute of Advanced Engineering, The Chinese University of Hong Kong, Shatin,
N. T., Hong Kong S. A. R., 999077, China

Z. Liang, X. Chen

Department of Electrical and Electronic Engineering, Southern University of Science and
Technology, Shenzhen, 518055, China

X. Fan, G. Wang

School of Physics, Beijing Institute of Technology, Haidian, Beijing, 10081 China

T. Ma

Department of Applied Physics, Hong Kong Polytechnic University, Hung Hom, Kowloon,
Hong Kong S. A. R., 999077, China

S. Gao

School of Instrumentation and Optoelectronic Engineering, Beihang University, Beijing
100191, China

E-mail: ghhu@ee.cuhk.edu.hk

Keywords: 1T' MoTe₂, entropy noise, true random numbers, secure cryptography, privacy safeguarding.

Abstract

True random numbers play a critical role in secure cryptography. The generation relies on a stable and readily extractable entropy source. Here, from solution-processed structurally metastable 1T' MoTe₂, we prove stable output of featureless, stochastic, and yet stable conductance noise at a broad temperature (down to 15 K) with minimal power consumption (down to 0.05 μ W). Our characterizations and statistical analysis of the characteristics of the conductance noise suggest that the noise arises from the volatility of the stochastic polarization of the underlying ferroelectric dipoles in the 1T' MoTe₂. Further, as proved in our experiments and indicated by our Monte Carlo simulation, the ferroelectric dipole polarization is a reliable entropy source with the stochastic polarization persistent and stable over time. Exploiting the conductance noise, we achieve the generation of true random numbers and demonstrate their use in common cryptographic applications, for example, password generation and data encryption. Besides, particularly, we show a privacy safeguarding approach to sensitive data that can be critical for the cryptography of neural networks. We believe our work will bring insights into the understanding of the metastable 1T' MoTe₂ and, more importantly, underpin its great potential in secure cryptography.

1. Introduction

Cryptography is of critical importance in the modern electronics era when the exponentially growing data is at risk of being attacked and sabotaged ^[1]. Secure cryptographic strategies are thus being sought for ^[1]. Random numbers, a string of random bits, play a central role in this. Amongst them, the random numbers generated using the entropy noise harnessed from the physical systems, such as the thermal noise, charge dynamics in semiconductors, oscillator jitters, and delays in microelectronic circuits ^[2], are particularly promising for extensive secure cryptography, as the entropy noise is intrinsically stochastic and the random numbers generated are truly random and cannot be predicted or reproduced ^[3]. However, harnessing the entropy noise from the physical systems can be energy consuming, and the entropy noise can be vulnerable to ambient noise and cryogenic attacks, undermining its reliability for true random number generation ^[4].

Intriguingly, the advances in nanomaterials science present new exciting opportunities for true random number generation. Quantum phenomena widely presented in nanomaterials, such as quantum tunnelling, electron correlation and electron-phonon interactions, and the *Rashba* effect, are proven inherently unpredictable ^[5-7] and, as discussed, the unpredictability can be a

key attribute of entropy for secure cryptography. State-of-the-art research shows that two-dimensional (2D) materials hold great interest for secure cryptography in modern electronics, given their unique material properties and the possibility for integration and synergy with modern electronics [2,8]. Particularly, with atomic thickness and innate quantum confinements, 2D materials can present stochasticity in the underlying electronic, optoelectronic, and photonic processes, as well as the chemical structures, giving rise to stable and readily extractable entropy noise [9–12]. For example, molybdenum ditelluride (MoTe_2) is one type of transition metal dichalcogenide, and, interestingly, in the mono- and few-layer forms MoTe_2 can appear as trigonal prismatic-orthorhombic (2H-1T) intermediate monoclinic (1T') phase [13]. The inherent structural metastability in the 1T' phase, along with the atomic thickness and innate quantum confinement, can induce volatile, stochastic polarization of the ferroelectric dipoles and as such, reliable entropy noise in the electronic properties of MoTe_2 [14]. Studies suggest that the structural metastability can even be resilient to ambient environmental, thermal, and electromagnetic disturbances [15,16], manifesting the potential of harnessing the entropy noise from 1T' MoTe_2 for reliable random number generation.

Here, we report true random number generation using structurally metastable 1T' MoTe_2 . We prepare the 1T' MoTe_2 via electrochemical exfoliation of the counterpart bulk, and probe the conductance noise from electrical characterizations as the entropy source. Particularly, we prove featureless, stochastic, and yet stable conductance noise output at a broad temperature spanning 15 K to 300 K, with an ultralow power consumption of down to $0.05 \mu\text{W}$. Our characterizations and statistical analysis of the characteristics of the conductance noise suggest that the noise arises from the volatility of the stochastic polarization of the ferroelectric dipoles in the 1T' MoTe_2 . As proved by our electrical characterizations and further indicated by our Monte Carlo simulation of the ferroelectric dipole polarization process, the polarization is a reliable entropy source with the stochastic polarization persistent and stable over time. Exploiting the conductance noise, we achieve true random number generation, and demonstrate cryptographic applications in password generation and data encryption. Furthermore, we show an interference and proffer safeguarding of neural networks using the random numbers, proving a novel privacy protection measure for sensitive data that can be critical for the cryptography of neural networks.

2. Results

2.1. 1T' metastable MoTe_2

MoTe₂ is a 2D layered transition metal dichalcogenide material. In its stable form, MoTe₂ predominantly exhibits a semiconducting trigonal prismatic (2H) lattice structure^[17] – the monolayer consists of a plane of hexagonally bonded Mo atoms sandwiched between two planes of Te atoms via chemical bonds. However, as schematically illustrated in Fig. 1a, the 2H MoTe₂ can have local lattice distortions along the *y*-axis, where the Te atoms form an octahedral coordination around the Mo atoms to give an alternating Te-Mo-Te stacking^[18,19]. This leads to a phase transition from 2H to a trigonal prismatic-orthorhombic (2H-1T) intermediate monoclinic phase (1T')^[18]. Different from the stable 2H phase, studies show that this intermediate 1T' phase can present structural metastability involving substantial instabilities in the underlying electronic structures^[20]. Specifically, as the electronic properties are governed by the electronic structures^[21,22], the structural metastability of the 1T' MoTe₂ can lead to stochastic noise in the electronic properties, for instance, the material electrical conductance (referred to as conductance). Here we aim to exploit the conductance noise from the 1T' MoTe₂ arising from its structural metastability as the entropy source for the generation of true random numbers.

1T' MoTe₂ can be produced through physical and chemical engineering processes, such as defect doping, electrostatic modulation, and strain engineering^[23–25]. Solution-based techniques facilitate high-yield, low-temperature, and cost-effective production of 2D materials^[26,27]. Given this consideration, and the integration capability of the solution-processed 2D materials with the semiconducting manufacturing and emerging printing technologies for practical cryptographical applications^[26,27], we prepare the 1T' MoTe₂ by electrochemical exfoliation, following the method reported in Ref. (28) (see Methods). Briefly, as illustrated in Fig. 1b, in a typical electrochemical exfoliation process, bulk MoTe₂ and platinum are used as the electrodes, and tetrahexylammonium cation (THA) dispersion in dimethylformamide (DMF) is used as the electrolyte. Upon exfoliation, the organic molecule THA intercalates into the bulk MoTe₂ and as such, weakens the van der Waals forces and expands the interlayer spacing, leading to the exfoliation of nanosheets from the bulk with mild sonication^[28]. Figure 1c shows a solution of the as-exfoliated MoTe₂.

We use transmission electron microscopy (TEM) to assess the structural and morphological characteristics of the as-exfoliated MoTe₂ nanosheets. Figure 1d shows the morphology of typical nanosheets of a few layers and a large cross-sectional area (~500 nm), suggesting that the electrochemical exfoliation has been successfully implemented to exfoliate the MoTe₂. Figure 1e presents a high-resolution TEM image of a typical nanosheet, revealing a lattice

spacing of 3.4Å and a non-hexagonal atomic structural arrangement. This indicates a 1T' phase of the as-exfoliated MoTe₂ nanosheets^[28]. Further electron diffraction pattern proves a non-hexagonal rhombic but a tetragonally symmetric lattice structure, confirming the 1T' phase of the as-exfoliated MoTe₂. Meanwhile, complementary X-ray photoelectron spectroscopic (XPS) analysis demonstrates 33.28:66.72 (in %) for the Mo and Te atoms in the as-exfoliated MoTe₂ nanosheets (Fig. S1), suggesting that the electrochemical exfoliation process leads to minimal defects and that the 1T' phase primarily arises from exfoliation-induced lattice distortions. We anticipate that the 1T' MoTe₂ can exhibit the conductance noise required for the true number generation.

2.2. 1T' MoTe₂ conductance noise

To probe the conductance noise from the 1T' MoTe₂, we fabricate a vertical device with the 1T' MoTe₂ sandwiched between gold electrodes, as shown in Fig. 2a (see Methods). This simplest device structure allows convenient current-voltage measurement. Upon measurement, the noise probed in the device current output can be considered as the conductance noise from the 1T' MoTe₂. Note that owing to solution processing, the device fabrication is scalable with a high yield (>90%); Fig. 2b. The cross-sectional scanning electron microscopic and elemental analyses prove clear 1T' MoTe₂/Au interfaces; Fig. 2c, d.

We first assess the conductance noise from the 1T' MoTe₂ at room temperature. Figure 2e shows the device current output at 0.05 V, and Fig. S2a-h show the outputs at 0.01-5 V. As observed, the device proves a featureless, stochastic, and yet stable noise in the current outputs at all the different voltages and, notably, an ultralow voltage of 0.05 V is sufficient to probe the substantial current output noise, i.e. the conductance noise of the 1T' MoTe₂. To further investigate the pattern and distribution of the conductance noise, we calculate the transient gradients of the current outputs, i.e. the difference between two neighboring current states divided by the time interval. As demonstrated in Fig 2g and Fig. S2i-p, the gradient histograms all establish Gaussian distributions with the gradients. This shows that the conductance noise indeed has no distinctive features from a statistical perspective, proving a high degree of unpredictability and randomness^[3]. As such, the featureless gradient distribution profiles imply that the conductance noise may be well suited to the true random number generation^[29]. Considering the potential exposure to the cryogenic attacks, we now extend the assessment from room temperature to low and even cryogenic temperature temperatures (down to 15 K). As proved in Fig. 2f, the device again proves a featureless, stochastic, and yet stable noise in

the current outputs at all the low and cryogenic temperatures. The gradient histograms estimated from the current outputs also establish Gaussian distributions; Fig. 2h-j. This demonstrates that the conductance noise from the 1T' MoTe₂ may be exploited as a reliable entropy source even at cryogenic temperatures. We conclude that the above assessments demonstrate the possibility of probing and extracting the conductance noise from the 1T' MoTe₂ with minimal power consumption with reliable results at cryogenic temperatures.

The noise from thermal and electronic systems stands as a primary entropy source for true random number generation ^[30]. Yet, as discussed, harnessing the noise demands substantial energy costs ^[4]. To exclude that the conductance noise demonstrated above originates from the ambient noise from thermal and the electrical characterization system, we concurrently assess the ambient noise by characterizing a blank sample. As clearly shown by the grey current outputs in Fig. 2e, f, the ambient noise distinctly deviates from the current noise (smaller by several orders of magnitude), though the ambient noise is also featureless, stochastic, and yet stable. As such, though taking the interference from the ambient noise into account, the origin of the conductance noise is primarily attributed to the intrinsic metastable properties of the 1T' MoTe₂.

2.3. Origin of the current noise

Studies show that the non-centrosymmetric lattice distortions in the monoclinic 1T' MoTe₂ can induce ferroelectric properties ^[14], and that the structural metastability can induce volatile, stochastic polarization of the underlying ferroelectric dipoles ^[31]. From our above conductance noise investigations, we infer that the conductance noise originates from the intrinsic metastable properties of the 1T' MoTe₂. Herein, we hypothesize that the conductance noise arises from the volatile, stochastic ferroelectric dipole polarization in the 1T' MoTe₂.

We present in Fig. 3a the current output of a typical MoTe₂ device at 0.05 V and 300 K and the corresponding cumulative charge in the sampling time-step intervals (note the minimal sampling time-step is 0.067 s). The cumulative charge may correspond to the polarization of the ferroelectric dipoles in the 1T' MoTe₂ ^[32]. We therefore intend to study the cumulative charge characteristic to understand the polarization behavior of the ferroelectric dipoles. As observed, the cumulative charge also proves a featureless, stochastic, and yet stable noise, indicating that the polarization of the ferroelectric dipoles is volatile and stochastic. We further use the weighted time-lag method, a technique widely adept at analyzing the random telegraph

noise^[33], to statistically evaluate the noise in the cumulative charge. Briefly, as plotted in Fig. 3d, the distribution of the cumulative charge is defined with a weighted time-lag, $TL = \lg\left(K \sum_n^{N-1} \frac{1}{2\pi\alpha^2} \exp\left(-\frac{[(Q_n-x)^2+(Q_{n+1}-y)^2]}{2\alpha^2}\right)\right)$, where Q_n and Q_{n+1} are the cumulative charge states at the n -th and $(n+1)$ -th moments, (x, y) denotes the corresponding coordinates in the TL plot, N is the total number of the moments, and α and K are the fitting parameters to ensure that the maximum of TL plot before logarithm equals to 1. Note that the cumulative charge states in the plot are distributed in ascending order, and that a TL approaching 0 means a stronger correlation between the cumulative charge state with the next state. As observed, the TL plot establishes a uniform, stochastic, and bimodal aggregation distribution along the diagonal, with both the larger and smaller cumulative charge states having a stronger correlation with their next states, and the medium cumulative charge states having a weaker correlation. Considering the polarization of the ferroelectric dipoles, this indicates that the ferroelectric dipoles are uniformly distributed with bimodal aggregations, and that the strongly polarized dipoles may require a strong current (i.e. the cumulative charge in our investigation) to reverse. Importantly, the uniform, stochastic distribution pattern suggests the polarization of the ferroelectric dipoles in the 1T' MoTe₂ is volatile and stochastic³⁴.

To exclude that the above noise in the cumulative charge and the distribution pattern of the TL plot originate from the ambient noise, we again concurrently assess a blank sample. As shown in Fig. 3b, e, the cumulative charge shows stable fluctuations accompanied by certain unstable spikes, while the TL plot establishes a monostable aggregation pattern with weak correlations in the cumulative charge states. This proves that the distinctly different characteristics in the cumulative charge and TL plot of the 1T' MoTe₂ device are primarily governed by the intrinsic material properties of the 1T' MoTe₂. Besides, we also assess a device fabricated with liquid-phase exfoliated MoS₂ (see Methods). MoS₂ is also a layered transition metal dichalcogenide material, but structurally stable with a centrosymmetric lattice structure^[34]. MoS₂ is reportedly used in true random number generation for cryptography based on a charge trapping and de-trapping mechanism in the MoS₂ material^[35,36]. Indeed, as clearly shown in Fig. 3c, the current output and the corresponding cumulative charge present the typical characteristics of charge trapping and de-trapping^[35]. The TL plot, as shown in Fig. 3f, establishes a few random aggregation regions with strong correlations in the cumulative charge states, which may be a result of charge trapping and de-trapping. The comparison of the cumulative charge characteristics and TL plots between the 1T' MoTe₂ and MoS₂ devices suggests that the non-

centrosymmetric lattice distortions of the 1T' MoTe₂ give rise to the volatile, stochastic polarization of the ferroelectric dipoles.

Our above investigation and analysis favor our hypothesis that the conductance noise arises from the volatile, stochastic polarization of the ferroelectric dipoles in the 1T' MoTe₂, as schematically illustrated in Fig. 3g. We conduct Monte Carlo simulation of the polarization of the ferroelectric dipoles (see Methods). Based on our hypothesis, we assume that the ferroelectric dipoles in the 1T' MoTe₂ are uniformly and stochastically distributed, and that the ferroelectric dipoles undergo stochastic reverses. Upon conductance noise probing of a 1T' MoTe₂ device with a constant bias, the volatile, stochastic polarization of the ferroelectric dipoles and the stochastic reverses can lead to fluctuations in the bound charges and as such, the conductance noise. Based on the Monte Carlo simulation, the current output is stable over a prolonged period with featureless and stochastic noise, consistent with the experiment testing, as shown in Fig. 3h. This indicates that the stochastic and volatile polarization of the ferroelectric dipoles is persistent and stable over time, and suggests the potential of exploiting the conductance noise as a reliable entropy source for true random number generation.

2.4. True Random number generation

To harness the above conductance noise from the 1T' MoTe₂ for true random number generation, we design a circuit as illustrated in Fig. 4a. Briefly, the circuit consists of a 1T' MoTe₂ device, an I/V converter, a high-pass filter, a comparator, and a Non-Linear Feedback Shift Register (NLFSR) module. Upon operation, the I/V converter transforms the current signal from the 1T' MoTe₂ device into a voltage signal that is convenient for subsequent processing. As shown in Fig. 4b, the voltage signal, i.e. 'output 1', demonstrates a voltage profile with featureless, stochastic, and yet stable noise. This proves that the circuit has captured the conductance noise from the 1T' MoTe₂. The gradients of the voltage signal statistically establish a Gaussian distribution, as shown in Fig. 4c, again demonstrating that the voltage signal has no distinctive features statistically. As discussed, again, a featureless gradient distribution implies that the voltage signal with the noise may be well suited to the true random number generation^[29]. The voltage signal is then passed through the high-pass filter to extract the noise in the form of differentiated stochastic voltage spikes, as shown by the 'output 2' in Fig. 4b. The gradients of the voltage spikes also establish a Gaussian distribution, as shown in Fig. 4d, again implying that the noise retains the featureless randomness and may therefore be well suited to the true random number generation. The comparator then processes the stochastic

voltage spikes to yield a voltage output in the form of a binary number string of 0's and 1's, as shown by the 'output 3' in Fig. 4b (see Fig. S3 for a zoomed-in distribution of the 0's and 1's in the time domain). As observed, the binary number string shows a random distribution of the 0's and 1's, with a ratio of $\sim 1:1$ (Fig. 4e). This indicates the binary number string generated from the circuit is random and potentially useful for secure cryptography.

To verify that the binary number string is truly random, we test its randomness using the National Institute of Standards and Technology (NIST) randomness testing suite. As presented in Table 1, the binary number string successfully passes the randomness test without post-processing. This proves the true randomness of the binary number string, and that the binary number string can be used in secure cryptographic applications [37]. However, the throughput of the true random binary number string is only approximately 10 bit/s, limiting its practical usefulness in high-throughput secure cryptographic applications. To address this limitation, employing a common approach for cryptographic random number generation [38], we use the true random binary number string as the seed, and then introduce the true random binary number string to an NLFSR module for high-throughput output of random binary number string with a data rate of, say, 1 Mbit/s, as shown in Fig. 4a. See the circuit design of the NLFSR in Fig. S4. As a demonstration, we present a high-throughput random binary number bitmap in Fig. S5.

2.5. Privacy safeguarding

The high-throughput random binary numbers generated can be used in secure cryptographic applications. For example, we show in Fig. S6 and Supplementary Video 1 the generation of one-time and strongly randomized passwords, relying on the unpredictability provided by the random numbers. Besides the password generation, data encryption can also make use of the unpredictability provided by the random numbers. We show in Fig. S7 and Supplementary Video 2 and 3 the use of the random numbers in the encryption (and decryption) of video and audio files. More explicitly, the encryption begins with integrating the random numbers into a mature encryption algorithm (e.g. AES encryption) to produce a unique key for encryption [39,40], and the encryption key is then used to encrypt (and decrypt) the data. The effectiveness of this data encryption approach lies in the fact that the encryption key is virtually impossible to predict or reproduce, thereby reducing the chances of successful brute-force attacks [41,42].

Besides the above common cryptographic applications, the importance of secure cryptography using the random numbers is magnified by the rapid advancements of the neural networks. In the context of machine learning and artificial intelligence using neural networks, adversarial

attacks pose a significant threat to data privacy^[43]. Here we adopt a differential data privacy safeguarding strategy and investigate the effectiveness of this approach to obfuscate the sensitive data in neural networks^[44]. As schematically shown in Fig. S8, the differential data privacy framework injects random numbers as the noise to the target data for encryption. Following this approach, we first train a Residual neural network (Resnet) model for pet cat recognition (Fig. 5a; see Methods). Resnets are a widely used neural network framework in image and pattern recognition^[45]. After training, the model can perform successful pet recognition with an accuracy of 92%. Note that the confusion matrix and detailed performance (including the training and validation accuracy and loss) of the well-trained Resnet variant model are shown in Fig. S9.

We then inject the random numbers as the noise to the target validation data. Interestingly, as shown in Fig. 5a, taking the image of a Siamese cat for demonstration, the noise perturbation appears negligible to the human eyes, manifesting that the random numbers as a minor and almost imperceptible noise perturbation to the data. This is ascribed to the innate ability of the human brain to process visual information holistically, i.e. focusing on the broader picture rather than the minute details^[46]. However, as demonstrated in Fig. 5b, the noise perturbation substantially affects the recognition of the well-trained Resnet variant model at all the different convolution layers. As shown in Fig. 5c, d, the confusion matrix (see also Fig. S10 for the confusion matrix details) and the accuracy (~78%) show the Resnet variant with the noise perturbation has a relatively poor performance in recognition. Particularly, comparing the accuracies with and without the noise perturbation, as shown in Fig. 5d, a little noise perturbation can cause a substantial degradation in the classification accuracy. This is because the noise disrupts the feature detection capability of the well-trained Resnet variant model in the initial layers of the network, which is then propagated to the deeper layers, leading to the exacerbation of the error^[47]. The further detailed difference (i.e. Δ) between the two success rates in the different 37 categories can be found in Fig. 5e. The findings prove that injecting the random numbers as noise perturbations that are not discernible to the human eyes can substantially interfere with the neural networks and as such, enhance the data privacy.

3. Conclusion

In this work, we have reported true random number generation using structurally metastable 1T' MoTe₂. The 1T' MoTe₂ is produced via a scalable, low-cost, and low-temperature solution-based electrochemical exfoliation approach. To extract the entropy noise from the 1T' MoTe₂,

we develop solution-processed devices from the 1T' MoTe₂, and probe the variations in the current output as the conductance noise. We prove a featureless, stochastic, and yet stable noise at a broad temperature spanning from 15 K to 300 K, with an ultralow power consumption of down to $\sim 0.05 \mu\text{W}$. Through detailed characterizations, statistical analysis of the characteristics of the conductance noise, and Monte Carlo modelling of the ferroelectric dipoles in the 1T' MoTe₂, we understand that the conductance noise arises from the volatility of the stochastic polarization of the underlying ferroelectric dipoles in the 1T' MoTe₂, and that the polarization is a reliable and robust entropy source. Taking advantage of the conductance noise, we design a simplified circuit to extract and convert the conductance noise for the generation of random numbers. The random numbers generated successfully pass the NIST test, demonstrating true randomness. Using the true random numbers as the seed, we achieve high throughput random number generation with a rate of 1 Mbit/s, and demonstrate their practical secure cryptographic applications, such as password generation and data encryption.

Beyond the common cryptographic applications, we have demonstrated privacy safeguarding of sensitive data in neural networks using the random numbers. Neural networks are a technology widely used in machine learning and artificial intelligence to undertake tasks in, for instance, image recognition, healthcare, autonomous driving, manufacturing, monitoring, and even defense, where sensitive data can be constantly involved. Our safeguarding approach therefore can serve as a novel privacy protection measure to avoid the leakage of the critical data without causing destructive interferences to the neural networks. Given this, and the scalability of solution processing, our approach of true random number generation using structurally metastable 1T' MoTe₂ holds great potential enabling secure neural networks.

4. Experimental Methods

Material exfoliation and device fabrication: Raw MoTe₂ and MoS₂ and all the other chemicals are purchased from Alpha Aeser and Sigma-Aldrich, and are used as received. The electrochemical exfoliation and ink formulation of MoTe₂ follow the method reported in Ref. (28). The liquid-phase exfoliation and ink formulation of MoS₂ follow the method reported in Ref. (27). For device fabrication, the Au/MoTe₂/Au and Au/MoS₂/Au devices are fabricated on Si/SiO₂ wafer, where the MoTe₂ and MoS₂ are deposited by spin coating, and the gold electrodes are deposited by electron-beam evaporation. The electron-beam evaporator is IVS EB-600. The MoTe₂ and MoS₂ after deposition are baked at 400 °C for 0.5 hours under nitrogen.

Electrical characterizations: Tektronix Keithley 4200-SCS parameter analyzer is used to measure the electrical characteristics of the devices under 300 K. For the 15 K, 100 K, and 200 K tests, FS-Pro is used under vacuum ($\sim 10^{-6}$ mbar).

Monte Carlo simulation: Assuming a constant electric field, the change in the polarization of the ferroelectric dipoles will not affect the field, but the internal polarization state of the ferroelectric dipoles in the 1T' MoTe₂ will change. The fluctuation of the polarization can lead to fluctuating bound charges, which can in turn cause fluctuations in the conductance state of the 1T' MoTe₂.

The polarization can switch between two states, i.e. P_1 and P_2 , and the switching follows the Arrhenius law [48]. The polarization can thus be modelled as a Poisson process, meaning that the probability of a switch in a small interval of time dt is given by $\lambda * dt$, where λ is the rate of the process. The rate follows the Arrhenius law, given by $\lambda = A * \exp(-E/(k * T))$, where A is the pre-exponential factor, E is the energy barrier, k is the Boltzmann constant, and T is the temperature. However, the switch in polarization now results in fluctuations in the bound charge instead of a change in the electric field. The bound charge ρ_B is related to the polarization P by the relation $\rho_B = -divP$, where div is the divergence operator, indicating that the bound charge is related to the spatial variation of the polarization. In a simple one-dimensional case, this can be described as $\rho_B = -dP/dx$. Now assume that the change in polarization is uniform across the material, the bound charge will change by $\Delta\rho_B$ proportional to the change in polarization ΔP , expressed as $\Delta\rho_B = -\Delta P/L$, where L is a characteristic length scale of the system. This change in voltage can cause a current to flow.

We propose that the change in the bound charge affects the resistance R of the material. A simple model assumes that the resistance is inversely proportional to the absolute value of the bound charge, $R = R_0/\rho_B$, where R_0 is a constant initial resistance. Finally, apply a constant voltage V across this variable resistor, the current I through the material at any time would be given by Ohm's law, $I(t) = V/R(t)$. The charge from the current can be described by $Q_i = \int_{t=i}^{t=i+1} dI/dt$. So every time the polarization switches, it will change the bound charge, which will then change the resistance and hence, the current fluctuations.

Consider a common effect often found in materials known as Poole-Frenkel behavior [49], the current through the material (and hence the resistance) is affected by the applied electric field (which in our case can be linked to the bound charge), and the current density J is given by $J =$

$J_0 * \exp(\beta * \sqrt{\varepsilon})$, where J_0 is the current density at zero field, ε is the electric field, and β is a material constant. In our scenario, we now link the bound charge and the electric field ε . Assume that the change in the bound charge $\Delta\rho_B$ is proportional to the change in electric field $\Delta\varepsilon$, the bound charge is expressed by $\Delta\rho_B = -\Delta\varepsilon/L$. Then, the current density will be dependent on the bound charge. Note that the *sqrt*(ε) means that this is not a simple linear or inversely proportional relationship.

Neural network recognition: The neural network security is carried out in Python 3 and is based on the Resnet framework. The Resnet variant is based on a Resnet 34 structure, consisting of convolution layers, residual blocks, and so on. The information about the Resnet 34 can be found at: <https://pytorch.org/vision/main/models/generated/torchvision.models.resnet34.html>. The public dataset is from the Visual Geometry Group at the University of Oxford (available at <https://www.robots.ox.ac.uk/~vgg/data/pets/>). The dataset consists of a 37-category pet dataset with roughly 200 images for each class with different scales, poses, and lighting. All the images have an associated ground truth annotation of breed, head ROI, and pixel-level trimap segmentation, and those are used for training and testing.

References

- [1] H. Jiang, D. Belkin, S. E. Savel'Ev, S. Lin, Z. Wang, Y. Li, S. Joshi, R. Midya, C. Li, M. Rao, M. Barnell, Q. Wu, J. J. Yang, Q. Xia, *Nat Commun* **2017**, *8*.
- [2] M. Lanza, A. Sebastian, W. D. Lu, M. Le Gallo, M. F. Chang, D. Akinwande, F. M. Puglisi, H. N. Alshareef, M. Liu, J. B. Roldan, *Science (1979)* **2022**, *376*.
- [3] S. Pironio, A. Acín, S. Massar, A. B. De La Giroday, D. N. Matsukevich, P. Maunz, S. Olmschenk, D. Hayes, L. Luo, T. A. Manning, C. Monroe, *Nature* **2010**, *464*, 1021.
- [4] M. Soucarros, J. Clédière, C. Dumas, P. Elbaz-Vincent, in *Journal of Electronic Testing: Theory and Applications (JETTA)*, **2013**, pp. 367–381.
- [5] N. Abraham, K. Watanabe, T. Taniguchi, K. Majumdar, *ACS Nano* **2022**, *16*, 5898.
- [6] G. Kim, J. H. In, Y. S. Kim, H. Rhee, W. Park, H. Song, J. Park, K. M. Kim, *Nat Commun* **2021**, *12*.
- [7] B. Liu, Y. F. Chang, J. Li, X. Liu, L. A. Wang, D. Verma, H. Liang, H. Zhu, Y. Zhao, L. J. Li, T. H. Hou, C. S. Lai, *ACS Nano* **2022**, *16*, 6847.
- [8] M. C. Lemme, D. Akinwande, C. Huyghebaert, C. Stampfer, *Nat Commun* **2022**, *13*, 1392.
- [9] C. Wen, X. Li, T. Zanotti, F. M. Puglisi, Y. Shi, F. Saiz, A. Antidormi, S. Roche, W. Zheng, X. Liang, J. Hu, S. Duhm, J. B. Roldan, T. Wu, V. Chen, E. Pop, B. Garrido, K. Zhu, F. Hui, M. Lanza, *Advanced Materials* **2021**, *33*.
- [10] A. Wali, H. Ravichandran, S. Das, *ACS Nano* **2021**, *15*, 17804.
- [11] N. R. Glavin, R. Rao, V. Varshney, E. Bianco, A. Apte, A. Roy, E. Ringe, P. M. Ajayan, *Advanced Materials* **2020**, *32*, 1904302.
- [12] M. I. Wafa, Y. M. El-Batawy, S. A. El-Naggar, *Opt Quantum Electron* **2021**, *53*, 261.
- [13] Z. Lai, Q. He, T. H. Tran, D. V. M. Repaka, D. D. Zhou, Y. Sun, S. Xi, Y. Li, A. Chaturvedi, C. Tan, B. Chen, G. H. Nam, B. Li, C. Ling, W. Zhai, Z. Shi, D. Hu, V. Sharma, Z. Hu, Y. Chen, Z. Zhang, Y. Yu, X. Renshaw Wang, R. V. Ramanujan, Y. Ma, K. Hippalgaonkar, H. Zhang, *Nat Mater* **2021**, *20*, 1113.
- [14] S. Yuan, X. Luo, H. L. Chan, C. Xiao, Y. Dai, M. Xie, J. Hao, *Nat Commun* **2019**, *10*, 1775.
- [15] D. H. Keum, S. Cho, J. H. Kim, D. H. Choe, H. J. Sung, M. Kan, H. Kang, J. Y. Hwang, S. W. Kim, H. Yang, K. J. Chang, Y. H. Lee, *Nat Phys* **2015**, *11*, 482.
- [16] Y. Qi, P. G. Naumov, M. N. Ali, C. R. Rajamathi, W. Schnelle, O. Barkalov, M. Hanfland, S. C. Wu, C. Shekhar, Y. Sun, V. Süß, M. Schmidt, U. Schwarz, E. Pippel,

- P. Werner, R. Hillebrand, T. Förster, E. Kampert, S. Parkin, R. J. Cava, C. Felser, B. Yan, S. A. Medvedev, *Nat Commun* **2016**, 7.
- [17] W. Gerstner, W. M. Kistler, R. Naud, L. Paninski, *Neuronal Dynamics: From Single Neurons to Networks and Models of Cognition*, Cambridge University Press, **2014**.
- [18] F. Zhang, H. Zhang, S. Krylyuk, C. A. Milligan, Y. Zhu, D. Y. Zemlyanov, L. A. Bendersky, B. P. Burton, A. V. Davydov, J. Appenzeller, *Nat Mater* **2019**, 18, 55.
- [19] Y. Wang, J. Xiao, H. Zhu, Y. Li, Y. Alsaïd, K. Y. Fong, Y. Zhou, S. Wang, W. Shi, Y. Wang, A. Zettl, E. J. Reed, X. Zhang, *Nature* **2017**, 550, 487.
- [20] Y. Cheon, S. Y. Lim, K. Kim, H. Cheong, *ACS Nano* **2021**, 15, 2962.
- [21] S. Tang, C. Zhang, C. Jia, H. Ryu, C. Hwang, M. Hashimoto, D. Lu, Z. Liu, T. P. Devereaux, Z.-X. Shen, S.-K. Mo, *APL Mater* **2017**, 6, 026601.
- [22] C. Zhang, W. Liu, F. Zhan, T. Zhang, L. Liu, M. Zhang, S. Xie, Z. Li, H. Sang, H. Ge, Y. Yan, R. Wang, Y. Wang, Q. Zhang, X. Tang, *Adv Funct Mater* **2021**, 31, 2103384.
- [23] K. Zhang, C. Bao, Q. Gu, X. Ren, H. Zhang, K. Deng, Y. Wu, Y. Li, J. Feng, S. Zhou, *Nat Commun* **2016**, 7.
- [24] J. Yang, J. Colen, J. Liu, M. C. Nguyen, G.-W. Chern, D. Louca, *Elastic and Electronic Tuning of Magnetoresistance in MoTe₂*, **2017**.
- [25] S. Cho, S. Kim, J. H. Kim, J. Zhao, J. Seok, D. H. Keum, J. Baik, D.-H. Choe, K. J. Chang, K. Suenaga, S. W. Kim, Y. H. Lee, H. Yang, *Phase Patterning for Ohmic Homojunction Contact in MoTe₂*, **n.d.**
- [26] G. Hu, J. Kang, L. W. T. Ng, X. Zhu, R. C. T. Howe, C. G. Jones, M. C. Hersam, T. Hasan, *Chem Soc Rev* **2018**, 47, 3265.
- [27] G. Hu, L. Yang, Z. Yang, Y. Wang, X. Jin, J. Dai, Q. Wu, S. Liu, X. Zhu, X. Wang, T.-C. Wu, R. C. T. Howe, T. Albrow-Owen, L. W. T. Ng, Q. Yang, L. G. Occhipinti, R. I. Woodward, E. J. R. Kelleher, Z. Sun, X. Huang, M. Zhang, C. D. Bain, T. Hasan, *A General Ink Formulation of 2D Crystals for Wafer-Scale Inkjet Printing*, **2020**.
- [28] W. Yu, Z. Dong, I. Abdelwahab, X. Zhao, J. Shi, Y. Shao, J. Li, X. Hu, R. Li, T. Ma, Z. Wang, Q. H. Xu, D. Y. Tang, Y. Song, K. P. Loh, *ACS Nano* **2021**, 15, 18448.
- [29] W. Yi, S. E. Savel'ev, G. Medeiros-Ribeiro, F. Miao, M.-X. Zhang, J. J. Yang, A. M. Bratkovsky, R. S. Williams, *Nat Commun* **2016**, 7, 11142.
- [30] D. Liu, Z. Liu, L. Li, X. Zou, *IEEE Transactions on Circuits and Systems II: Express Briefs* **2016**, 63, 608.
- [31] A. Jindal, A. Saha, Z. Li, T. Taniguchi, K. Watanabe, J. C. Hone, T. Birol, R. M. Fernandes, C. R. Dean, A. N. Pasupathy, D. A. Rhodes, *Nature* **2023**, 613, 48.

- [32] N. W. Ashcroft, N. D. Mermin, *Solid State Physics*, Cengage Learning, **2022**.
- [33] J. Martin-Martinez, J. Diaz, R. Rodriguez, M. Nafria, X. Aymerich, *IEEE Electron Device Letters* **2014**, *35*, 479.
- [34] T. Chowdhury, J. Kim, E. C. Sadler, C. Li, S. W. Lee, K. Jo, W. Xu, D. H. Gracias, N. V Drichko, D. Jariwala, T. H. Brintlinger, T. Mueller, H.-G. Park, T. J. Kempa, *Nat Nanotechnol* **2020**, *15*, 29.
- [35] X. Ma, Y.-Y. Liu, L. Zeng, J. Chen, R. Wang, L.-W. Wang, Y. Wu, X. Jiang, *ACS Appl Mater Interfaces* **2022**, *14*, 2185.
- [36] H. Ravichandran, D. Sen, A. Wali, T. F. Schranghamer, N. Trainor, J. M. Redwing, B. Ray, S. Das, *ACS Nano* **2023**, *17*, 16817.
- [37] L. C. Meiser, J. Koch, P. L. Antkowiak, W. J. Stark, R. Heckel, R. N. Grass, *Nat Commun* **2020**, *11*.
- [38] K. S. Woo, Y. Wang, Y. Kim, J. Kim, W. Kim, C. S. Hwang, *Adv Electron Mater* **2020**, *6*.
- [39] M. J. Dworkin, E. B. Barker, J. R. Nechvatal, J. Foti, L. E. Bassham, E. Roback, J. F. Dray Jr, **2001**.
- [40] D. Kumar Sharma, N. Chidananda Singh, D. A. Noola, A. Nirmal Doss, J. Sivakumar, *Mater Today Proc* **2022**, *51*, 104.
- [41] S. Zhou, X. Wang, Y. Zhang, B. Ge, M. Wang, S. Gao, *Multimed Syst* **2022**, *1*.
- [42] A. J. Acosta, T. Addabbo, E. Tena-Sánchez, *International Journal of Circuit Theory and Applications* **2017**, *45*, 145.
- [43] H. Xu, Y. Ma, H. C. Liu, D. Deb, H. Liu, J. L. Tang, A. K. Jain, *International Journal of Automation and Computing* **2020**, *17*, 151.
- [44] C. Dwork, in *Automata, Languages and Programming* (Eds.: M. Bugliesi, B. Preneel, V. Sassone, I. Wegener), Springer Berlin Heidelberg, Berlin, Heidelberg, **2006**, pp. 1–12.
- [45] K. He, X. Zhang, S. Ren, J. Sun, in *Proceedings of the IEEE Conference on Computer Vision and Pattern Recognition*, **2016**, pp. 770–778.
- [46] S. Kvatinsky, K. Talisveyberg, D. Fliter, A. Kolodny, U. C. Weiser, E. G. Friedman, in *2012 IEEE 27th Convention of Electrical and Electronics Engineers in Israel*, IEEE, **2012**, pp. 1–5.
- [47] Z. Li, F. Liu, W. Yang, S. Peng, J. Zhou, *IEEE Trans Neural Netw Learn Syst* **2022**, *33*, 6999.

- [48] F. A. Modine, R. W. Major, S. I. Choi, L. B. Bergman, M. N. Silver, *J Appl Phys* **1990**, 68, 339.
- [49] J. L. Hartke, *J Appl Phys* **1968**, 39, 4871.

Figures

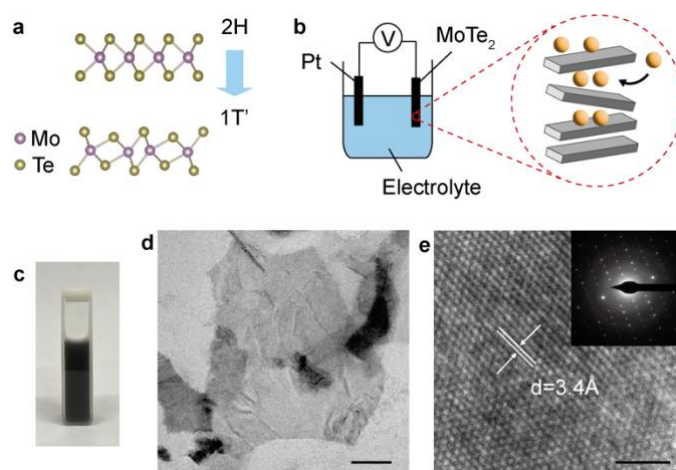


Figure 1. 1T' MoTe₂ by electrochemical exfoliation. (a) Schematic hexagonal symmetry and the distorted quadrilateral symmetry crystalline structures of 2H and 1T' MoTe₂, respectively. (b) Schematic electrochemical exfoliation of MoTe₂, and the schematic intercalation of molecular compounds between the MoTe₂ layers. Pt and MoTe₂ are used as the electrodes. (c) Image of an as-exfoliated MoTe₂ dispersion. (d, e) Transmission electron microscopic images of the as-exfoliated MoTe₂ nanosheets. Inset of (e) shows the selected electron diffraction pattern, proving a distorted quadrilateral symmetrical crystalline structure.

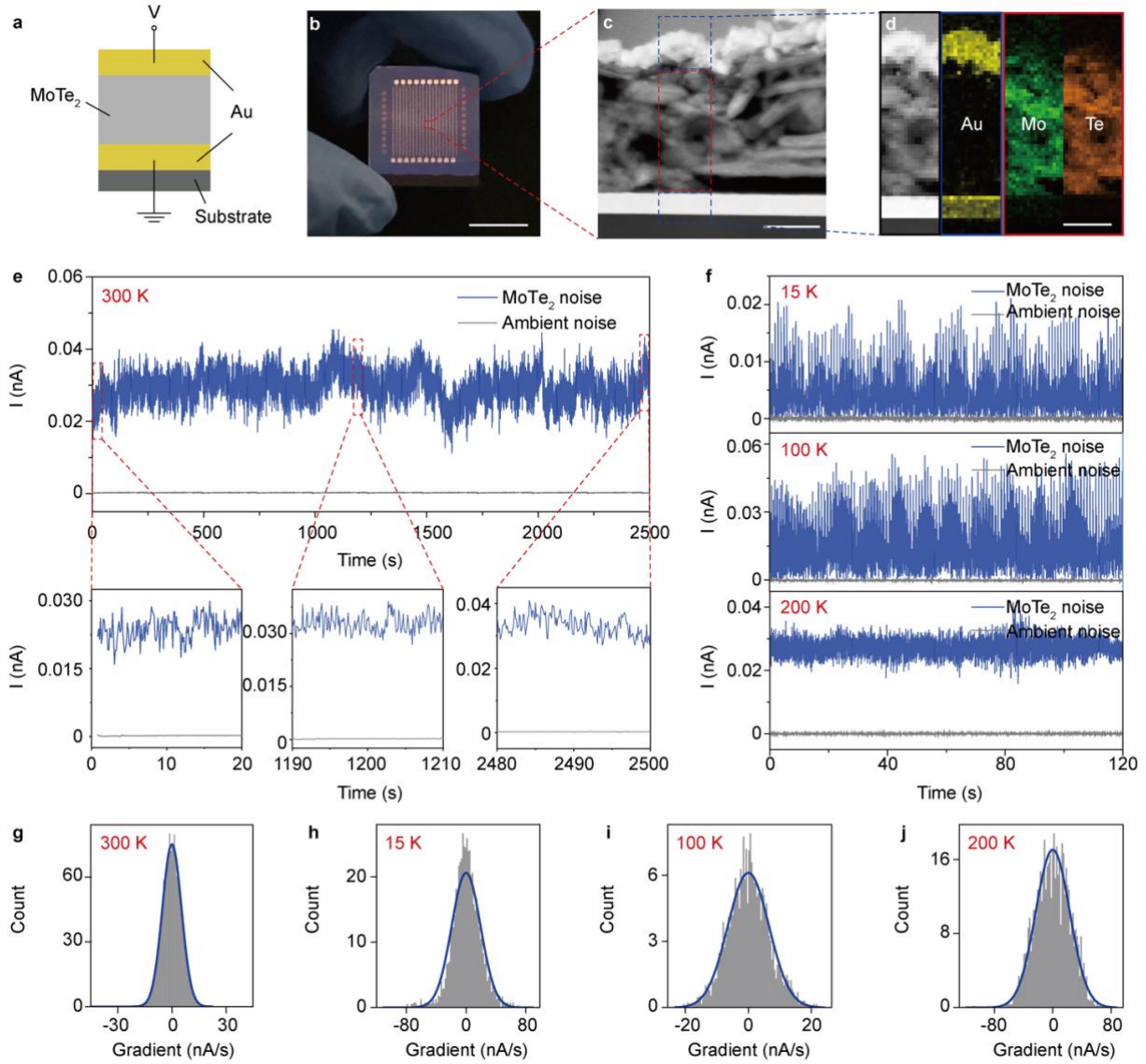


Figure 2. 1T' MoTe₂ device and the conductance noise. (a) Schematic configuration of the 1T' MoTe₂ device. MoTe₂ is sandwiched between e-beam evaporated gold electrodes. The substrate is Si/SiO₂. (b) Image of an array of 10 × 10 1T' MoTe₂ devices. (c) Cross-sectional scanning electron microscopic image of the device, and (d) the corresponding elemental analysis of the selected areas for the Au, Mo, and Te elements. (e) Current profile in blue as probed from a typical MoTe₂ device at 300 K, and the detailed current profiles at the different short periods. (f) Current profiles in blue as detected from the MoTe₂ device at the other temperatures. The operation voltage is 0.05 V. The current profiles from a blank sample are in grey. (g-j) The histograms and Gaussian fittings of the slope distributions from (e, f). The slope is obtained by dividing the current increment at each time step by the time interval. Scale bar – (b) 1 cm, (c) 300 nm, and (d) 300 nm.

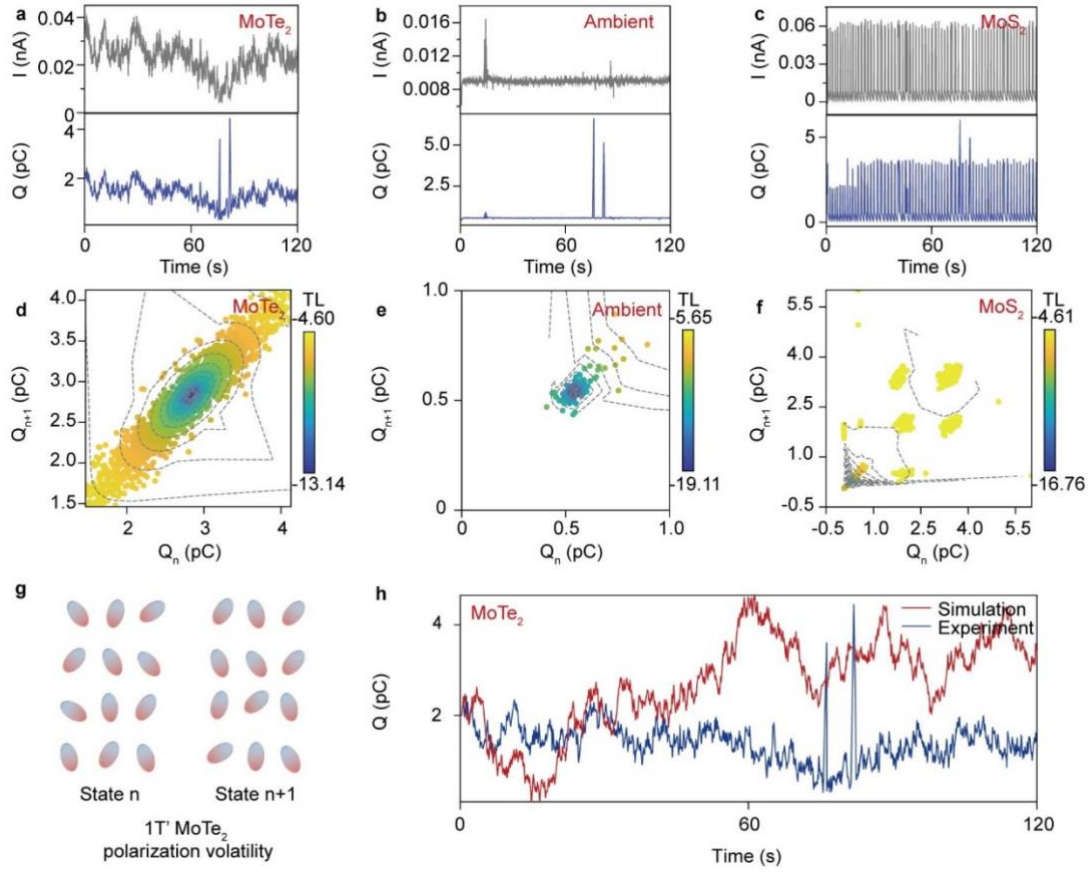


Figure 3. The origin of the conductance noise of 1T' MoTe₂. Current profiles and the corresponding cumulative charge fluctuations from (a) a typical 1T' MoTe₂ device, (b) a blank device, and (c) a MoS₂ device. The operation voltage is 0.05 V. The operation temperature is 300 K. The cumulative charge is integrated in the sampling time-step intervals. The minimal sampling time-step is 0.067 s. The time-lag plot for the cumulative charge fluctuations of (d) the MoTe₂ device, (b) the blank device, and (c) the MoS₂ device. (g) Schematic representation of the n -th and $(n + 1)$ -th polarization states of the underlying ferroelectric dipoles in the 1T' MoTe₂ in our proposed current noise mechanism, showing the volatility and stochasticity of the polarization of the ferroelectric dipoles. (h) The charge profile from the Monte Carlo simulation compared with the experimental charge profile from the 1T' MoTe₂ device.

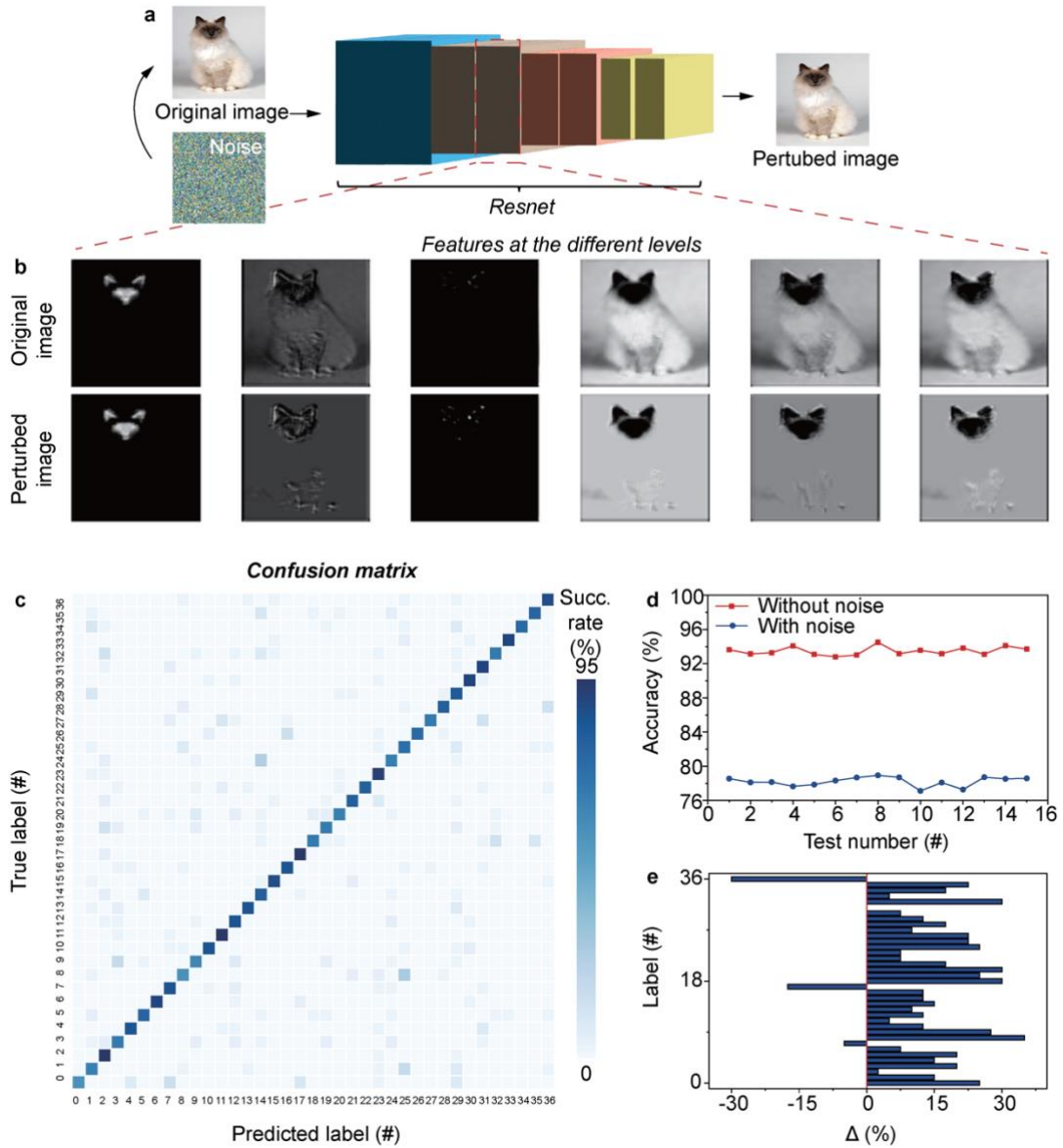


Figure 5. Interference and proffer safeguarding in neural networks. (a) Resnet variant architecture for the recognition of a cat without and with noise perturbation. The noise map is produced using the true random numbers generated. (b) The cat images without and with noise perturbation at the intermediate convolution layers, showing that the perturbed images lose certain features of the cat at the convolution layers. (c) Confusion matrix for the Resnet variant recognition with noise perturbation. The scale corresponds to the success rate of predicted labels. The x and y coordinates denote the predicted and true labels of the 37 different classifications in the training dataset. (d) The accuracy with and without noise perturbation at different numbers of tests. (e) The difference between the success rates in confusion matrices with and without noise perturbation along the diagonal. The y coordinate denotes the difference in the success rate on the diagonal, and the x coordinate the 37 different classifications. The confusion matrix with the success rate values is presented in Fig. S10.

Table 1. NIST test of the true random number generator.

#	Name	P-value	Success	Post-processing
01	Approximate entropy	1.0	Success	No
02	Block frequency	0.824	Success	No
03	Cumulative sums	0.728, 0.526	Success	No
04	FFT	0.041	Success	No
05	Frequency	0.823	Success	No
06	Linear complexity	-	-	Limited throughput
07	Longest run	0.445	Success	No
08	Non overlapping template	0.999	Success	No
09	Overlapping template	-	-	Limited throughput
10	Random excursions	-	Success	No
11	Random excursions variant	-	Success	No
12	Rank	-	-	Limited throughput
13	Runs	0.017	Success	No
14	Serial	0.499, 0.499	Success	No
15	Universal	-	-	Limited throughput

Supporting Information for

True random number generation using metastable 1T' molybdenum ditelluride

Yang Liu et al.

E-mail: ghu@ee.cuhk.edu.hk

This section contains:

Supplementary Figure S1-S10

Supplementary References

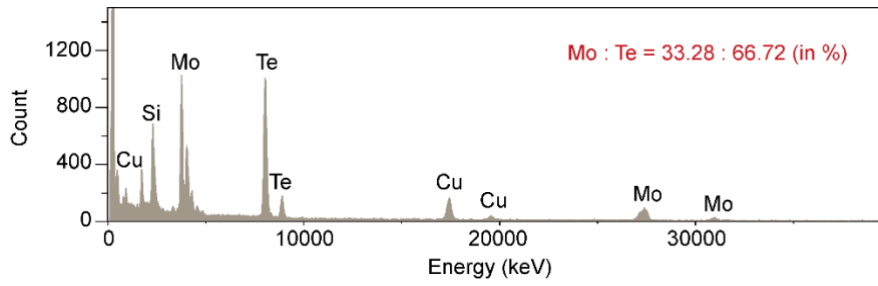


Figure S1. Analysis of the as-exfoliated 1T' MoTe₂ nanosheets. Energy dispersive X-ray spectrometry (EDS) element mapping of the as-exfoliated 1T' MoTe₂ nanosheets. The ratio of Mo and Te atoms is 33.28:66.72 (%), suggesting that there are minimal defects in the 1T' MoTe₂ nanosheets.

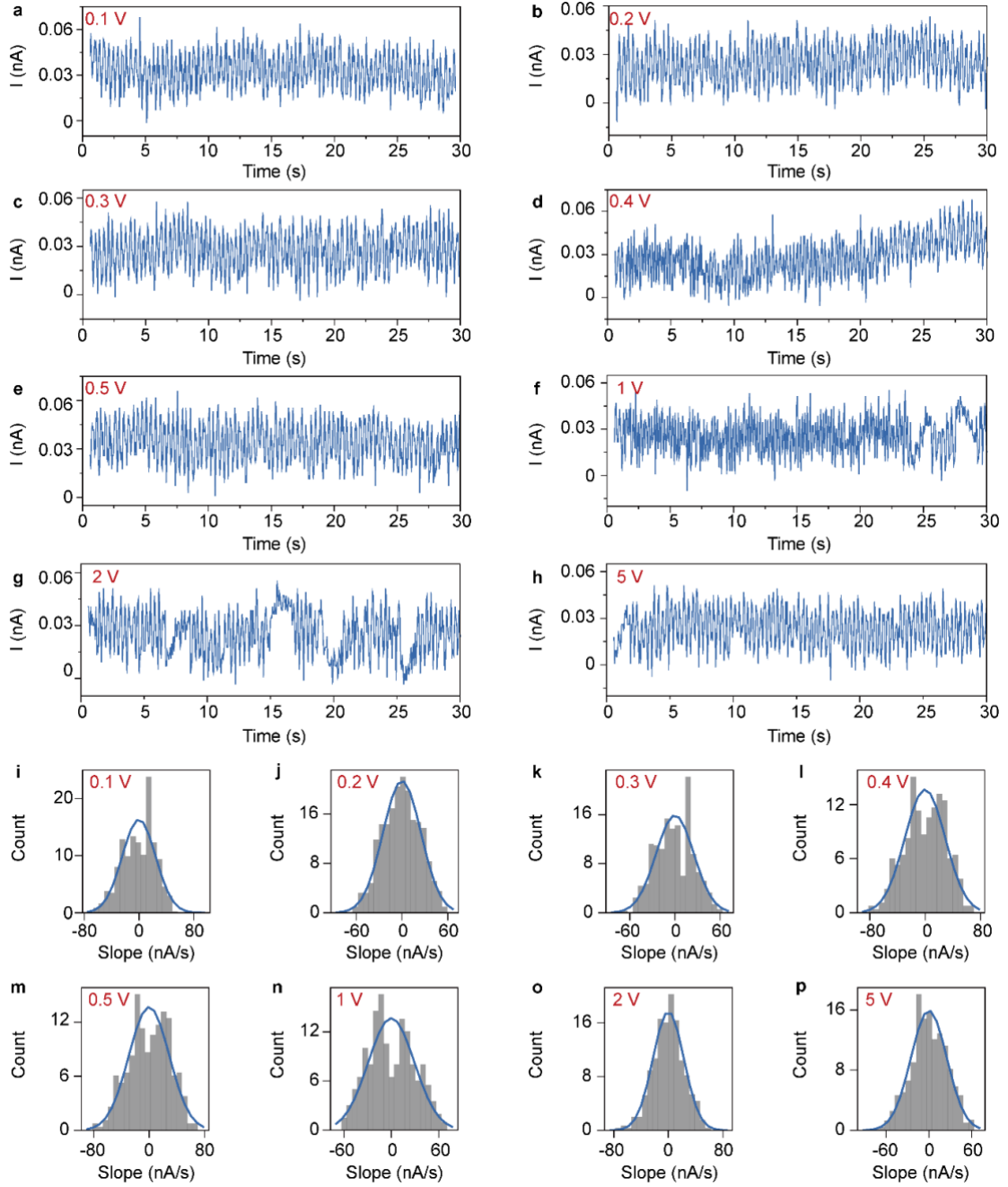


Figure S2. 1T' MoTe₂ conductance noise under the different voltages. (a)-(h) Current profiles of a typical 1T' MoTe₂ device at 0.1 V, 0.2 V, 0.3 V, 0.4 V, 0.5 V, 1 V, 2 V, and 5 V. Temperature 300 K. (i)-(p) The corresponding histograms and Gaussian fittings of the slope distribution. The slope is obtained by dividing the current increment at each time step by the time interval.

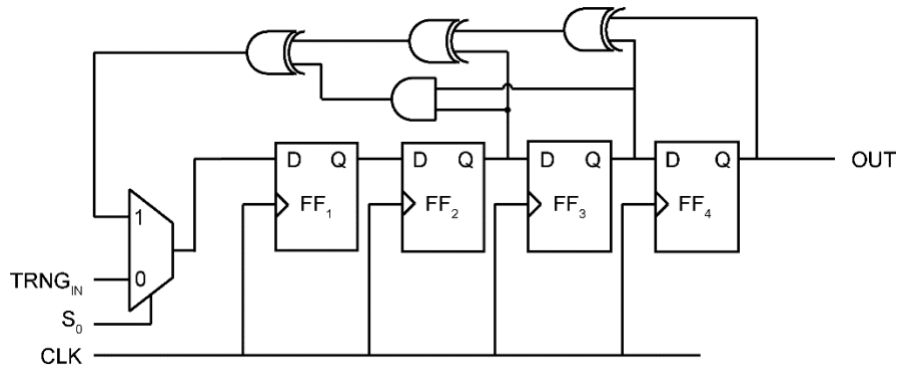


Figure S4. 4-bit nonlinear feedback shift register (NLFSR) circuit design. The random number sequence generated by the true random number generator in this work is used as the seed input. A high throughput random number sequence is obtained by setting a high clock frequency, e.g. 1 Mhz.

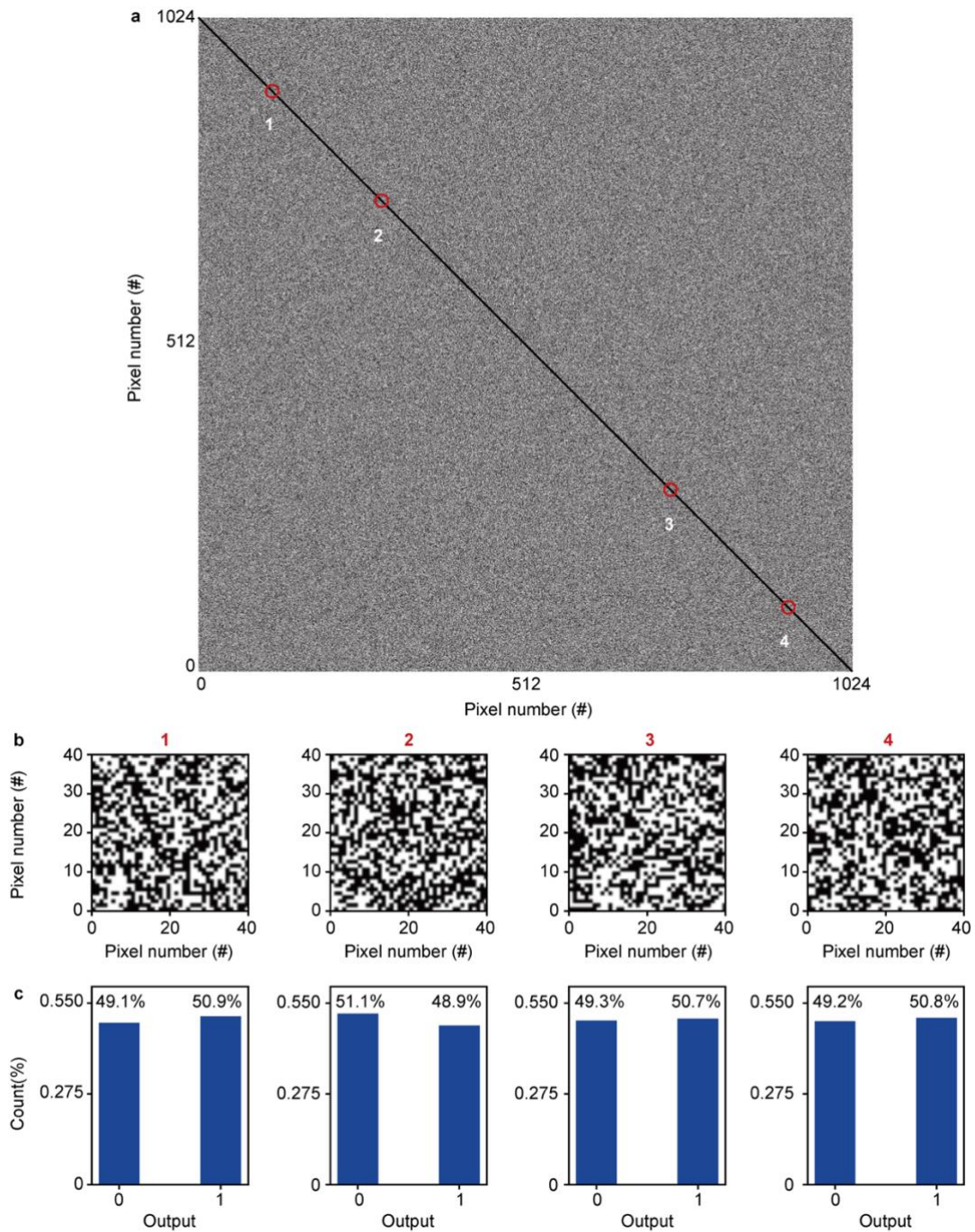


Figure S5. A 1024*1024 bitmap composed of a sequence of binary random numbers. (a) High-data-volume bitmap graph. Four randomly selected regions along the diagonal are shown in (b). (c) The corresponding histograms showing the distributions of the 0's and 1's. The ratios of the 0's and 1's are close to 1 to 1.

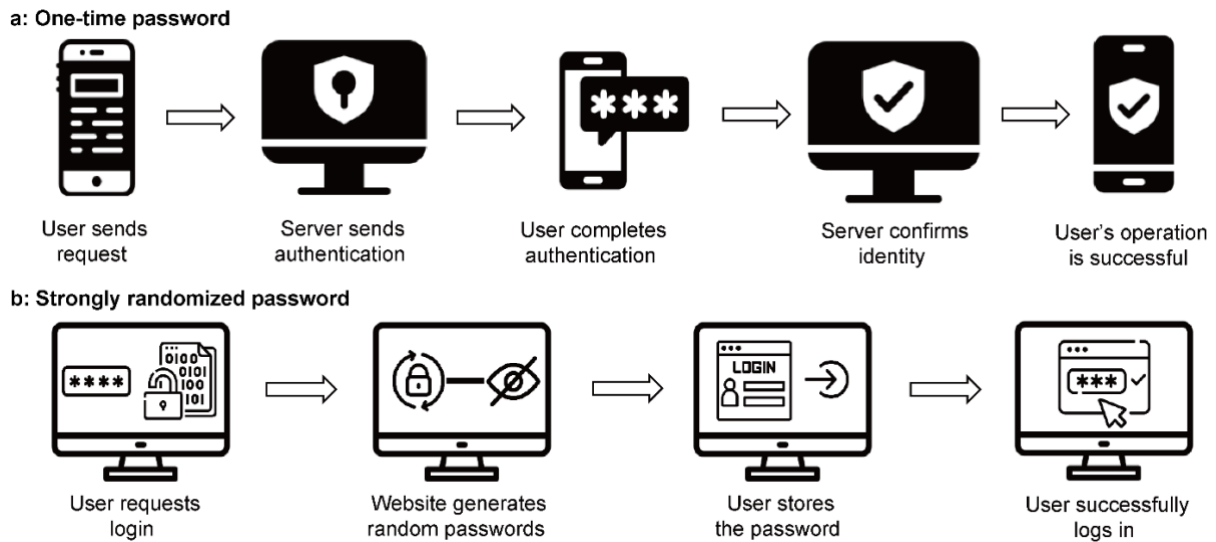


Figure S6. Password generation. (a) Schematic generation and the use of one-time password (OTP). OTP ^[1] is a unique code that is valid for only one login session and transaction. It is often used as a second factor in two-factor authentication (2FA) ^[2] and multi-factor authentication (MFA) ^[2] systems. (b) Schematic generation and the use of strongly randomized passwords. Strongly randomized passwords can be stored in systems for the application scenarios that require a high level of password security. Please the generation of the passwords in Supplementary Video 1.

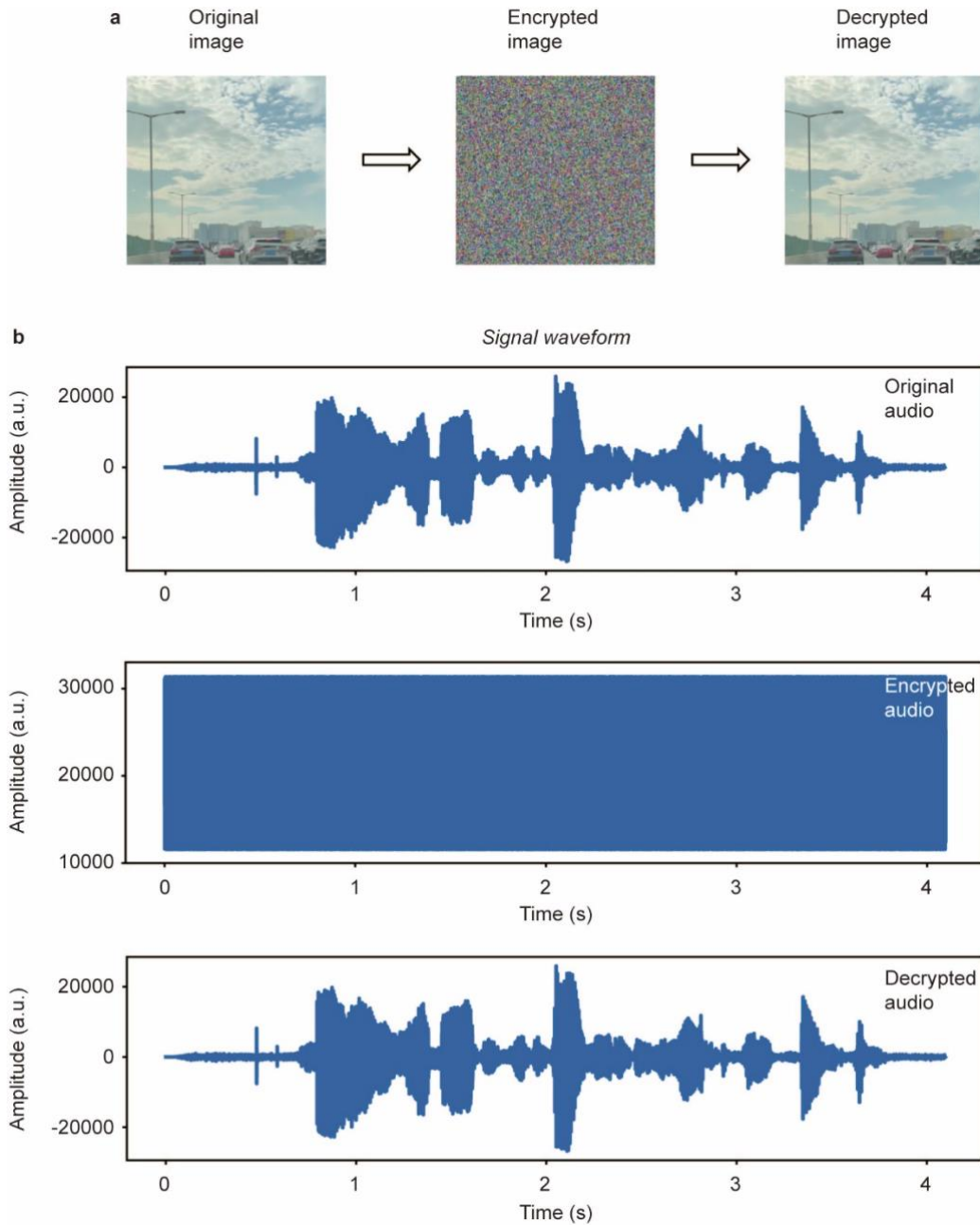


Figure S7. Data encryption. (a) Encryption and decryption of an image in Supplementary Video 2. The encryption and decryption processes are conducted by performing the common encryption/decryption operations (e.g., AES^[3] encryption/decryption, etc.) on the pixels of the images using the random numbers generated in this work. Our proposed method of encrypting and decrypting images is also applicable to other images. (b) Acoustic spectrograms for audio encryption and decryption, showing a four-second audio, the audio after bit-by-bit encryption, and the audio after decryption. Please the encryption and decryption of the video and audio in Supplementary Video 2 and 3.

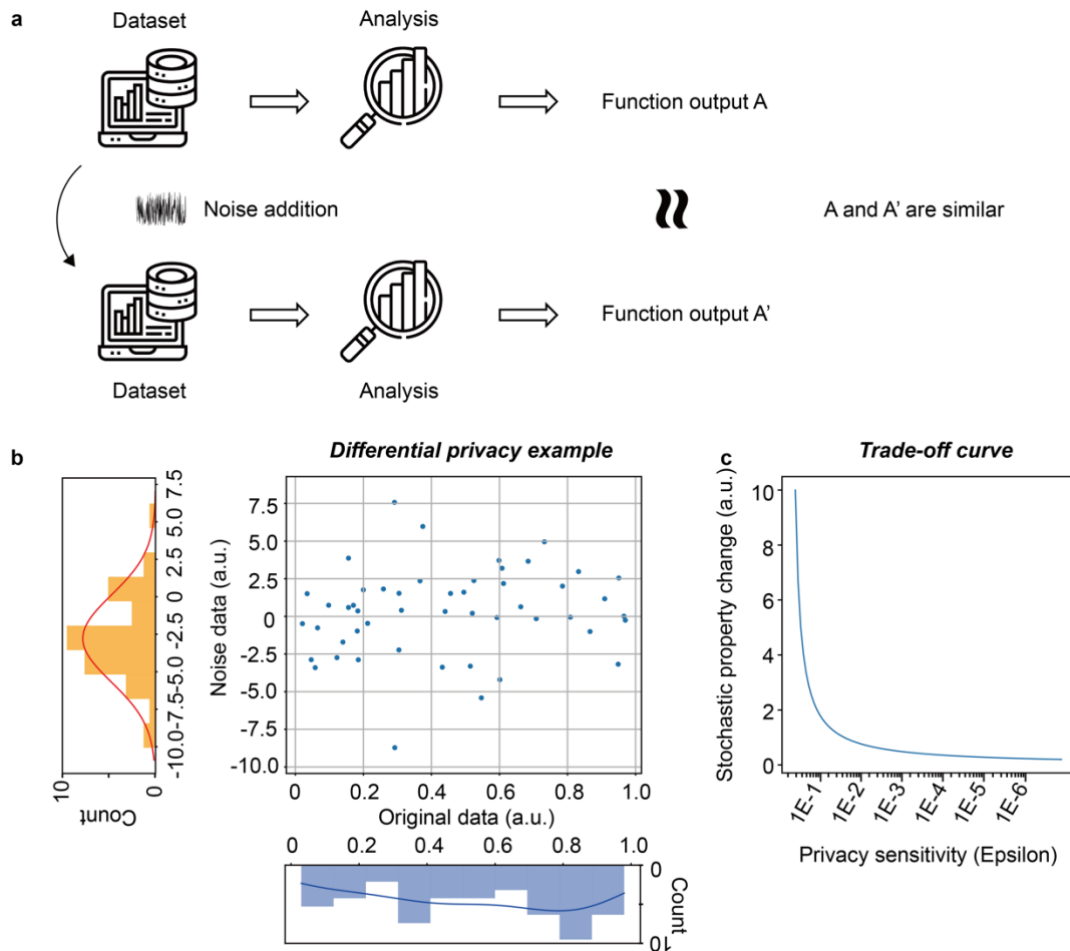


Figure S8. Data privacy protection strategy. (a) Differential data privacy workflow. Differential privacy is a robust framework used in statistical and machine learning analysis of datasets^[4]. The core idea is to ensure that the release of the data (or the statistics derived from the data) does not compromise the privacy of any individuals in the dataset, and that the dataset with the noise perturbation retains the key features. (b) A case example showing injecting noise to a dataset for data privacy protection. The left side shows the noise data, and the bottom side the original raw data. The noise data is injected into the original data. (c) The trade-off curve between the privacy sensitivity (*Epsilon*) and the stochastic property change. It is possible to achieve an optimal level of noise injection depending on the application scenarios.

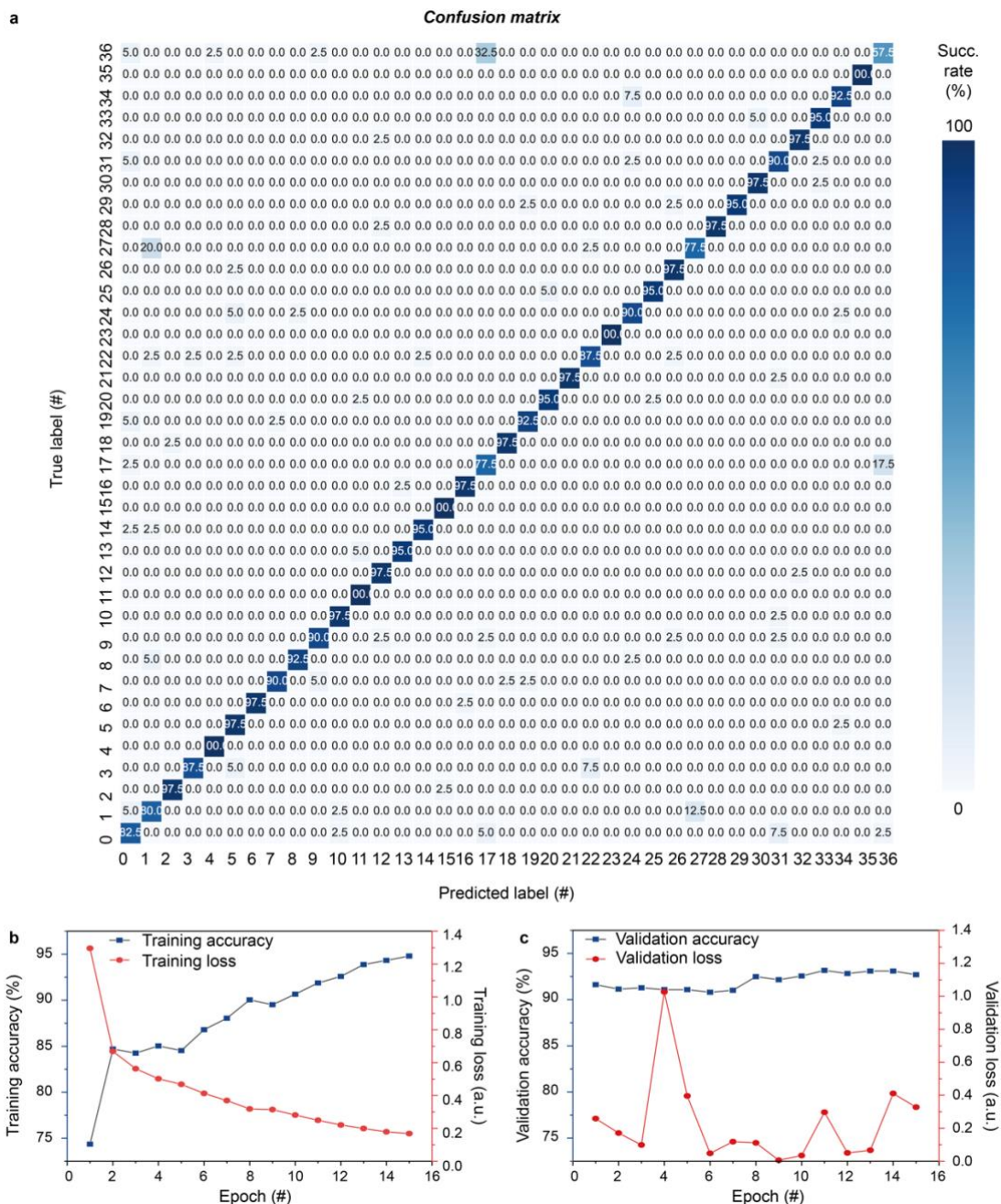


Figure S9. Confusion matrix without noise perturbation and the training performance of the Resnet model. (a) Confusion matrix without noise perturbation. The x and y coordinates denote the predicted and true labels of the 37 different classifications in the training dataset. The scale (i.e. the success rate of classification) corresponds to the ratio of the number of the correct predicted labels to the number of the true labels. The values shown in the confusion matrix represent the success rate of the predicted labels. The success rate shows that the trained Resnet variant achieves a good performance ($\sim 92\%$). (b) The training accuracy and training loss of the Resnet variant. (c) The validation accuracy and validation loss of the Resnet variant. Based on the performance of (b) and (c), it can be concluded that the Resnet variant is well-trained for the Oxford pet-iii dataset.

Supplementary References

- [1] N. Haller, C. Metz, P. Nesser, M. Straw, *A One-Time Password System*, **1998**.
- [2] A. Ometov, S. Bezzateev, N. Mäkitalo, S. Andreev, T. Mikkonen, Y. Koucheryavy, *Cryptography* **2018**, 2, 1.
- [3] M. J. Dworkin, E. B. Barker, J. R. Nechvatal, J. Foti, L. E. Bassham, E. Roback, J. F. Dray Jr, **2001**.
- [4] C. Dwork, in *Automata, Languages and Programming* (Eds.: M. Bugliesi, B. Preneel, V. Sassone, I. Wegener), Springer Berlin Heidelberg, Berlin, Heidelberg, **2006**, pp. 1–12.